Photoacoustics 4 (2016) 1–10

Contents lists available at ScienceDirect

Photoacoustics

journal homepage: www.elsevier.com/locate/pacs

Performance of a Multispectral Optoacoustic Tomography (MSOT) System equipped with 2D vs. 3D Handheld Probes for Potential Clinical Translation

Volker Neuschmelting [a,b], Neal C. Burton [c], Hannah Lockau [a], Alexander Urich [c], Stefan Harmsen [a], Vasilis Ntziachristos [d,e], Moritz F. Kircher [a,f,g,*]

[a] Department of Radiology, Memorial Sloan Kettering Cancer Center, New York, USA
[b] Department of Neurosurgery, University Hospital Cologne, Cologne, Germany
[c] iThera Medical GmbH, Munich, Germany
[d] Institute for Biological and Medical Imaging, Helmholtz Zentrum, Munich, Germany
[e] Chair for Biological Imaging, Technische Universität München, Germany
[f] Center for Molecular Imaging and Nanotechnology (CMINT), Memorial Sloan Kettering Cancer Center, New York, USA
[g] Department of Radiology, Weill Cornell Medical College, New York, USA

ARTICLE INFO

Article history:
Received 13 August 2015
Received in revised form 23 November 2015
Accepted 18 December 2015
Available online 25 December 2015

Keywords:
Handheld optoacoustic imaging
Photoacoustic imaging
Transcranial imaging
Melanoma
Brain metastasis

ABSTRACT

A handheld approach to optoacoustic imaging is essential for the clinical translation. The first 2- and 3-dimensional handheld multispectral optoacoustic tomography (MSOT) probes featuring real-time unmixing have recently been developed. Imaging performance of both probes was determined in vitro and in a brain melanoma metastasis mouse model in vivo. T1-weighted MR images were acquired for anatomical reference. The limit of detection of melanoma cells in vitro was significantly lower using the 2D than the 3D probe. The signal decrease was more profound in relation to depth with the 3D versus the 2D probe. Both approaches were capable of imaging the melanoma tumors qualitatively at all time points. Quantitatively, the 2D approach enabled closer anatomical resemblance of the tumor compared to the 3D probe, particularly at depths beyond 3 mm. The 3D probe was shown to be superior for rapid 3D imaging and, thus, holds promise for more superficial target structures.

1. Introduction

Multispectral optoacoustic tomography (MSOT) is an emerging real-time optical biomedical imaging technique, providing non-invasive, high resolution, intrinsic or contrast-enhanced, anatomical, functional and metabolic tomographic imaging at several centimeters of tissue depth [1]. In principle, a nanosecond laser pulse in the near-infrared (NIR) range induces molecules to thermoelastically expand due to photon absorption. This short-lasting expansion generates the emission of a pressure wave that is detected by an ultrasonic transducer and converted into an image [2]. Anatomical images are generated dependent on the absorption contrast of different tissue structures in single wavelength images. Multispectral images can yield metabolic information by resolving spectral signatures of intrinsic tissue molecules or extrinsically administered contrast agents absorbing at certain spectra. Intrinsically, imaging of lipids and melanin concentration as well as the oxygenation levels by oxygenated and deoxygenated hemoglobin has been implemented by spectral unmixing based on the unique signature of the components in the NIR spectrum [3–5]. Extrinsic contrast agents such as small molecule dyes, e.g. indocyanine green, fluorescent proteins or nanoparticles can significantly enhance the optoacoustic contrast, allow deeper tissue imaging and facilitate specific molecular processes to be imaged [6–9]. We previously have shown the potential of gold nanoparticles serving as a multimodal contrast agent in high grade glioma imaging [9]. However, these studies as well as previous multispectral optoacoustic tomography studies in various other small animal models in neuroimaging [4,8], cancer [10,11] and vascular disease research [12] so far have been based on complex

* Corresponding author at: Memorial Sloan Kettering Cancer Center, Department of Radiology, and Center for Molecular Imaging & Nanotechnology (CMINT), 1275 York Ave, New York, NY 10065, USA. Tel.: +1 646 888-3371; fax: +1 646 422-0408.
E-mail address: kircherm@mskcc.org (M.F. Kircher).

http://dx.doi.org/10.1016/j.pacs.2015.12.001

stagnant optoacoustic imaging devices for preclinical use only, not suitable for clinical translation [1,7]. Progress in the illumination and detector technology has led to experimental MSOT setups for potential handheld operation [13–16]. As a crucial step towards clinical application, a 2- and a 3-dimensional handheld MSOT probe have recently been developed, specifically designed with the aim of clinical translation. We studied the performance of these new MSOT handheld-probes in vitro and in vivo in a melanoma brain metastasis mouse model.

2. Material and methods

2.1. Handheld MSOT probe setup

The recently developed 3D cup-shaped handheld MSOT probe (iThera Medical, Munich, Germany) consists of an array of 384 ultrasonic detector elements that are arranged on a spherical surface with a radius of 40 mm towards the center of the sphere. It allows an optimized tomographic coverage angle of 120° with a center frequency of 4 MHz (Fig. 1A). The fractional bandwidth (6 dB) of the 3D detector was determined by the manufacturer to be on average 58% in transmit/receive mode. The array follows similar principles for 3D handheld optoacoustic tomography as previously reported [16], but increased the number of detector elements by 50% and the angular coverage by 30° to improve its capabilities for potential clinical translation. Silica fused-end fiber bundles for illumination are fixed in the center of the array and coupled onto a 120-grid 1.6 mm thick diffuser (Edmunds Optics Inc., Barrington, NJ, USA) for optimized scattered distribution of light within the field of view (FOV). The probe was integrated into a stage controlled water filled (deionized and degased) animal bed to control x,y,z translation during imaging, ensure constant temperature maintenance at 34 °Celsius as well as to facilitate stable acoustic coupling. A 0.1 mm thin transparent polyvinyl chloride membrane served as a cover and clear ultrasound gel as ultrasonic couplant.

The recently developed 2D arc-shaped handheld MSOT probe (iThera Medical, Munich, Germany) consists of a 2D array of 256 detector elements that are arranged along an arc on a spherical surface (radius = 40 mm). It results in a greater coverage angle of 135° at the same center frequency (4 MHz) (Fig. 1B). The manufacturer determined the fractional bandwidth (6 dB) of the 2D detector to be on average 52% in transmit/receive mode. The 2D probe was in principle based on a similar transducer array as previously reported [13], but was improved to allow for potential clinical applications, i.e. modifications to the size dimensions of the array to provide a greater coverage angle, increasing the number of detector elements by 50%, and adjusting the center frequency. The fused-end light fiber bundles that guide the laser beam are fixed next to the center of gravity of the detector array at a 10° angle to direct the illumination into the center of the FOV with the use of a 30° circular patterned diffusor (Luminit Co., Torrance, CA, USA) coupled in between to allow laser beam shaping for sufficiently even scattered light distribution. The shell of the probe is water filled (deionized and degased) and sealed watertight on the surface by a thin transparent polyethylene membrane towards the FOV to allow for acoustic coupling.

2.2. Illumination characterization

Both probes were connected to the same optoacoustic imaging platform EIP10 (iThera Medical, Munich, Germany) designed for experimental clinical use. This setup enabled quick plug-and-play switching of the two handheld probes. The illumination beam is

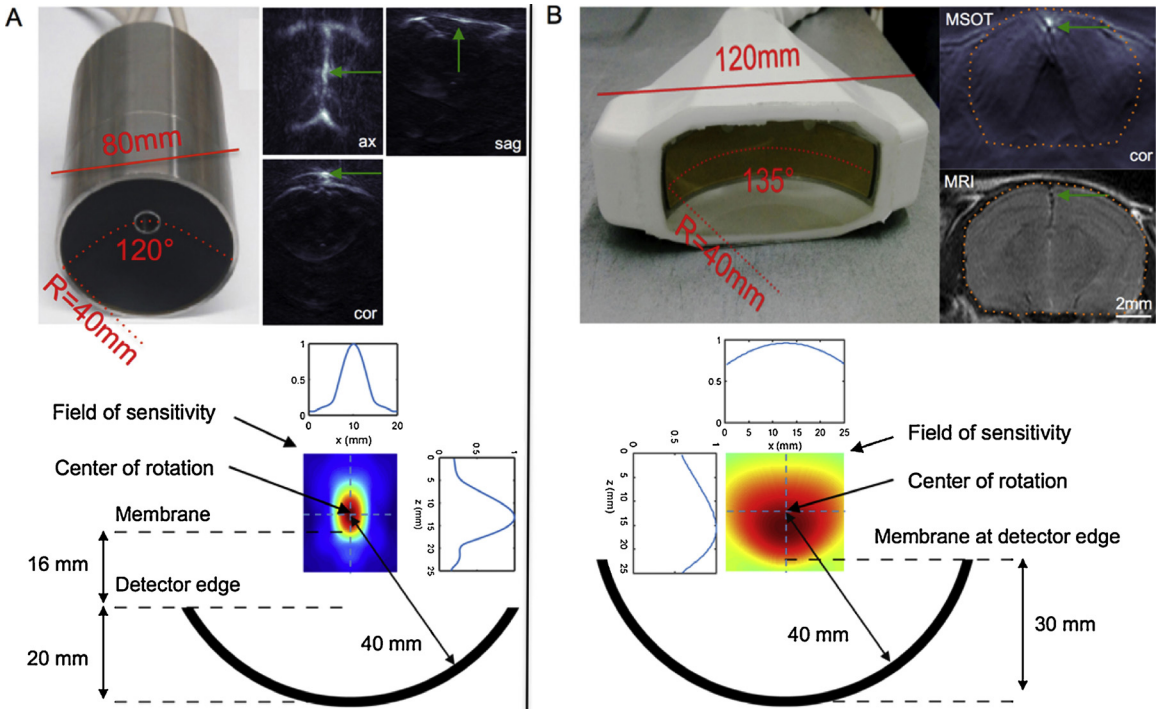

Fig. 1. A. Upper Panel: Configuration of the 3D-cup shaped handheld probe with a 384-element spherical detector array that covers an angle of 120°. The illumination source is fixed in the center of the array. The setup provides an axial (ax), sagittal (sag) and coronal (cor) image plane in one set as demonstrated here showing the superior sagittal sinus of a naïve mouse brain (green arrows). **Lower Panel:** The field of sensitivity around the center frequency (4 MHz) is shown. The center of rotation is 16 mm apart from the detector edge due to the cylindrical configuration of the detector array. **B. Upper Panel:** Configuration of the 2D-arc shaped handheld probe with a 256-element spherical detector array that covers an angle of 135°. In contrast to the 3D-approach it only allows acquisition of one image plane per image set, e.g. the coronal plane of a naïve mouse brain as shown here in reference to the corresponding coronal T2-weighted MRI (superior sagittal sinus = green arrow; brain circumference = dotted orange line). **Lower Panel:** This configuration allows a broader field of sensitivity around the center frequency (4 MHz) within the field of view.

generated by a wavelength-tunable (680-980 nm) optical parametric oscillator with a pulse duration of < 10 ns at a frame rate of 10 Hz. In 2D, the optoacoustic signal generated by a single laser pulse was simultaneously detected with the 256 detector elements, in 3D with the 384 detector elements. The illumination pattern of both probes was determined by translating an energy meter (EnergyMax-USB J-50MB-YAG, Coherent) with an additional aperture (3.5 mm in diameter) in front of the membranes of the two probes. The resulting fluence values were normalized to generate fluence maps. The measured illumination pattern was fitted with a 2D Gaussian function to determine the full width at half maximum (FWHM) in order to allow a comparison of the illumination pattern of both probes.

2.3. Resolution characterization

The resolution maps and the sensitivity fields were calculated with the use of the ultrasound simulation program Field II (http://field-ii.dk/) in MATLAB (MathWorks Inc, Natick, MA, USA). At first, the signals of an array of optoacoustic point sources within the field of view were simulated with Field II with the shape, the position, as well as the center frequency and bandwidth of individual detector elements being taken into account. The variation of the resulting signal amplitudes of the point sources corresponds to the sensitivity field of the detector array as shown in Fig. 1. The images of individual point sources were reconstructed from the simulated signals and the extension of the resulting point-spread function was characterized by its full width at half maximum (FWHM) along the direction with the largest extension. The resulting point spread function FWHM values of the simulated array of point sources were combined to form the resolution maps. In order to obtain the out-of-plane resolution of the 2D detector, optoacoustic point sources were simulated outside of the imaging plane. The out-of-plane resolution values were extracted from the FHWM of the signal amplitude variation of optoacoustic point sources with a varying distance to the imaging plane. In order to validate the simulation results, the resolution was measured using black polyethylene microspheres with an approximate diameter of 50 μm as previously described [16].

2.4. MSOT image acquisition and processing

MSOT images were acquired multispectrally according to the same protocol for both the 2D and 3D probe (21 wavelengths, 700-900 nm in 10 nm intervals, average of 5 frames per wavelength). While the field of view was set to 25 x 25 mm for the 2D probe, the field of view of the 3D probe was 10 x 10 x 25 mm (X x Z x Y). A pockels cell (Q-switch) delay (PCD) was increased from its optimal point to 250 μs to reduce the overall laser energy for the whole output spectrum in order to approximately meet the maximum permissible skin exposure in humans as reported in the American National Standard for Safe Use of Lasers [17] (2D: mean across wavelengths 21.3 ± 2.9 mJ/cm^2; 3D: mean 23.1 ± 3.1 mJ/cm^2; Fig. 2A). In order to compensate for different laser energies at different wavelengths, an internal laser energy meter reading was used. Both image data sets were reconstructed according to the same algorithm with the use of the back-projection method in ViewMSOT Software (V3.6, iThera Medical, Munich, Germany). After image reconstruction, images corresponding to different wavelengths were weighted with the internal laser energy values. The images were low and high pass filtered (50 kHz to 6.5 MHz) and the speed of sound was adjusted if appropriate: The natural round shape of small air bubble inclusions in the agarose allowed for the appropriate adjustment in vitro. In vivo, the round crossection of the prominent superficial sagittal sinus vein of the mice's brain in the coronal plane served as the target of appropriate speed of sound adjustment. Additionally, the 2D image data were corrected for depth (background: 0.1 cm^{-1} absorption, 70% oxygenation). After reconstruction, the images were spectrally decomposed by linear spectral unmixing on a pixel by pixel basis (negative values discarded) based on the individual absorption spectra of oxygenated and deoxygenated hemoglobin as well as melanin in the NIR window (Fig. 2B). This was done to analyze for the tissue content of melanin in all of the data as well as additionally for oxygenated and deoxygenated hemoglobin, respectively, for the in vivo data. Region of interest (ROI) analyses for MSOT signal intensities as well as ROI sizes were determined by an independent observer, blinded to the data acquisition.

2.5. In vitro model

A suspension of live B16F10 melanoma cells in phosphate buffered saline (PBS) (1.8×10^5 cells/20 μl PBS referred to OD[800 nm] = 1) was used in a 1.5%-agarose phantom (0.002%/vol. black ink and 1.2%/vol. 20%-intralipids added for scattering and absorption) approximately mimicking the optical properties of brain tissue in the NIR (absorption coefficient $\mu_a \approx 0.2$ cm^{-1}; reduced scattering coefficient ($\mu'_s \approx 10$ cm^{-1}) [18,19] to determine (1) the MSOT signal to concentration ratio of the cells in a dilution series with PBS serving as negative control; (2) the signal to tissue depth in increasing phantom thickness in relation to tissue mimicking background; and (3) signal linearity over time at constant cell concentration, constant tissue mimicking thickness (3 mm) and constant illumination energy level, respectively. The ROI sizes were set to a constant size for each probe to compare the signal intensities of the B16F10 cell suspensions to the signal of PBS and tissue mimicking background, respectively, as controls. The direct comparison of signal values between the two probes

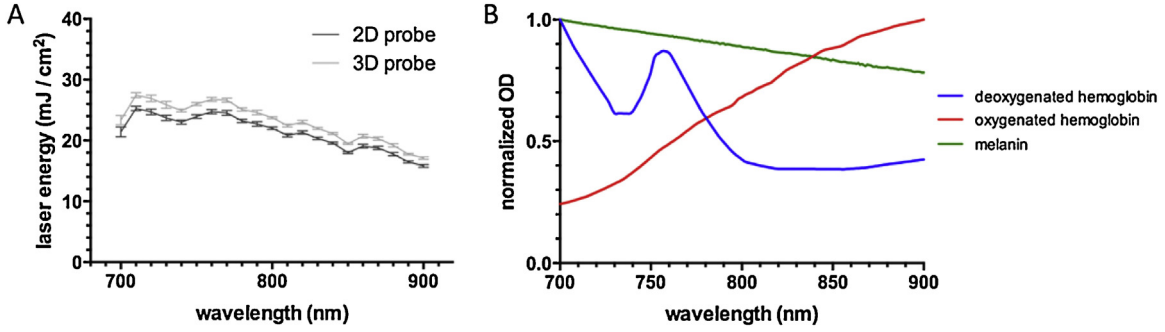

Fig. 2. A. The average laser energy output of the 2D and 3D probe across the NIR window with the PCD adjusted to 250 μs (mean ± SD represents n = 6 time points equally distributed throughout all experiments) **B.** The optical absorption spectra of deoxygenated, oxygenated hemoglobin and melanin used for spectral unmixing, normalized to their individual maximum OD within the wavelength range 700 to 900 nm.

was based on the normalization of the respective data to the signal of a constant absorber (OD = 1) that served as standard for both probes.

2.6. In vivo model

We chose to use a local melanoma brain metastasis model for this performance study due to (1) the excellent intrinsic optoacoustic contrast of melanin, (2) the challenging optical properties of brain tissue in situ, (3) well controllable, reproducible and uniform tumor generation by stereotactic implantation, and (4) because of its clinical relevance. In compliance with the local animal care and use committee, four female albino C57BL/6NTac-*Tyr*^{tm1Arte} were stereotactically implanted with $2x10^5$ isogeneic luciferase-transfected B16F10 melanoma cells (suspended in 2 μl PBS) into the right frontal lobe (1.0 mm posterior to bregma, 2.5 mm lateral to sagittal suture, at 2.5 mm depth). The mice developed spherical tumors of 3.5-7 mm in diameter within 13 days. MSOT was sequentially performed transcranially on days 6, 8, 10 and 13 to monitor tumor growth, using 2.0% isoflurane inhalation anesthesia. The 2D probe was rotated 90° in order to obtain perpendicular planes (coronal and sagittal). The tumor sizes were measured in their maximum extent in each dimension x, y, z based on unmixed melanin signal in one data set for the 3D probe while the image with the maximum tumor extent in each dimension was separately chosen out of the stack of images acquired with the 2D probe. The tumor extent was measured according to the stated dimensions x and z in the coronal plane, and the y dimension in the sagittal plane for both approaches. To determine the test-retest reliability, the same mice were imaged with the use of the 2D as well as the 3D probe on the same day under the same conditions by the same observer repetitively three times in a pseudo-randomized order (test 1, 2 and 3). The mice were fully removed from the field of view between scans. The mice were euthanized by carbon dioxide asphyxiation and the brain tissue including tumors were harvested and processed in 4% paraformaldehyde for further histological examination.

2.7. Magnetic resonance imaging (MRI)

Mouse brain 3D MR images were acquired in vivo on day 13 post implantation under 2.0% isoflurane inhalation anesthesia with the use of a 4.7-Tesla Bruker USR animal scanner (Biospec 47/40, Bruker Biospin Corp., Ettlingen, Germany) equipped with a 300 mT/m gradient coil (20 cm inner diameter) and a custom-built birdcage resonator (32 mm inner diameter): We obtained a 3D isovoxel T1-weighted gradient echo sequence (FLASH) (echo/repetition time (TE/TR) = 5.5/35 ms, FOV = 30x20x20 cm, matrix = 192x128x128, isotropic resolution = 156 μm, flip angle = 45°, averages = 4, acquisition time = 38.5 min) to serve as anatomical reference standard in vivo for tumor size evaluations as depicted by the maximum x and z dimensions of the tumor on the coronal plane as well as the maximum extent on the y dimension on the sagittal plane with the use of OsiriX software (V.5.5.1, Pixmeo, Geneva, Switzerland). The maximum extent of the tumor was defined on the basis of the T1 signal alteration of the tumor in relation to healthy mouse brain tissue in each plane.

2.8. Statistical analysis

Differences in MSOT signal intensities and ROI sizes between the data acquired by the 2D and 3D probe were calculated separately by the Student's *t*-test. Results were considered significant when P was < 0.05 (Bonferroni-corrected for multiple comparisons, if appropriate), as determined with the software Prism (V6.0, GraphPad Inc., CA, USA). With regard to testing for

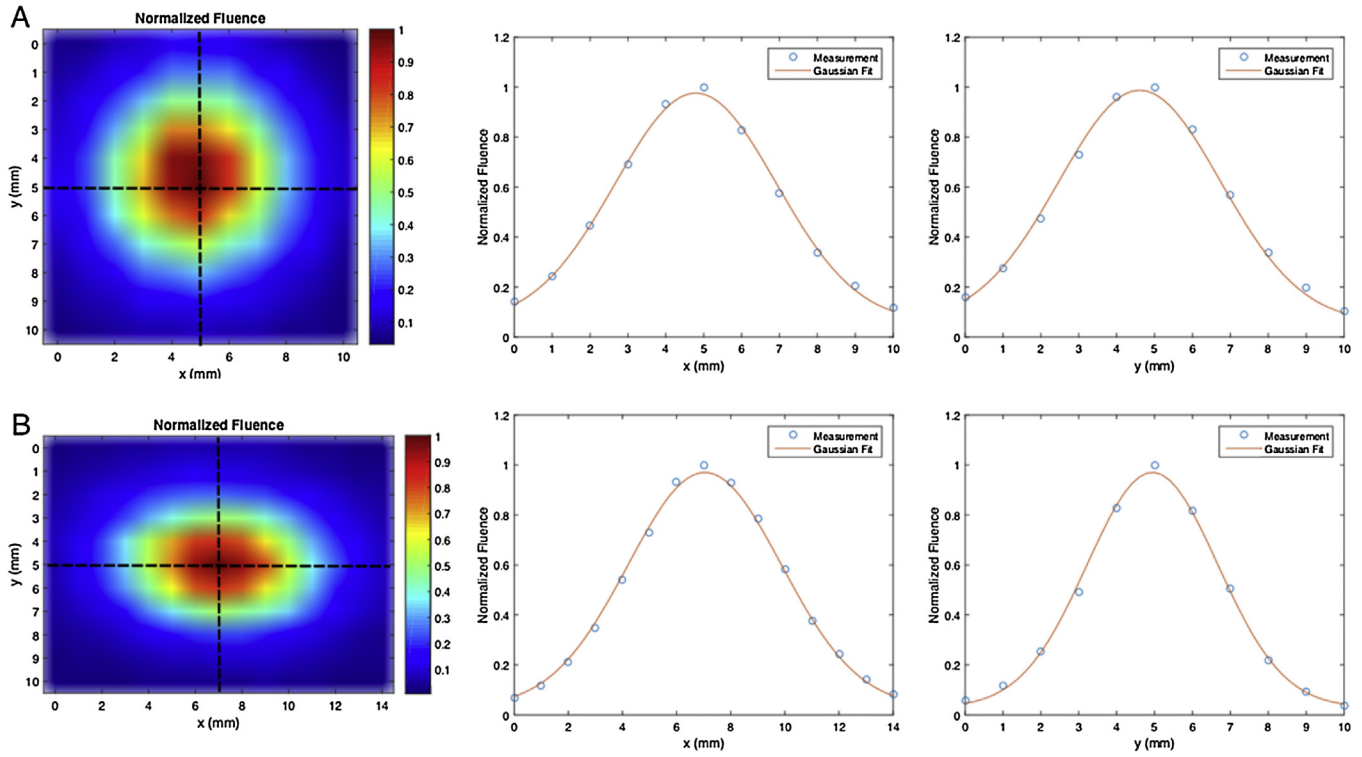

Fig. 3. A. Illumination pattern of the 3D probe: The fluence values are shown as a normalized fluence map. According to the 2D Gaussian fit, the FWHM of the symmetric light spot is 10 mm with the light spot being symmetric. Cross sections of the measured and fitted values around the probe output center along x and y are additionally shown. **B.** The illumination pattern of the 2D probe was found to be about 30% elongated in-plane and about 20% shortened out-of-plane compared to the symmetric light spot of the 3D probe.

precision in vivo, the test-retest reliability of the approaches was separately determined by the calculation of the intraclass correlation coefficient (ICC) and its 95%-confidence intervals (CI) [20]. The accuracy of the approaches in vivo was individually determined on the basis of tumor size resemblance in reference to the MRI as standard and expressed as bias and its 95% limits of agreement (LA) according to the Bland-Altman procedure [21].

3. Results

3.1. Fluence maps

The illumination pattern of the 3D probe was found to be a symmetrical light spot with a FWHM of 10 mm (Fig. 3A). The FHWM of the 2D probe's illumination pattern was found to be 13.3 mm in the x dimension (elongated in-plane) and 8.1 mm for the y dimension (shortened out-of-plane) (Fig. 3B). Overall, the illuminated areas are very similar for both probes with the difference of the areas above half maximum to be below 3%.

3.2. Resolution maps

At the center of rotation the optimal resolution of the 2D transducer was found to be at approximately 200 μm and, thus, slightly higher than the optimal resolution of the 3D probe (approximately 240 μm) (Fig. 4A and B). While the in-plane resolution of the 2D probe was found to be stable ± 10 mm around the center of rotation in the x and z plane (Fig. 4B), the 3D probe's resolution gradually decreases with respect to distance from the center of rotation (Fig. 4A). In the y dimension (slice thickness) however, the 2D probe's out-of-plane resolution dramatically decreases beyond approximately ± 1 mm out-of-plane (Fig. 4B) while the resolution of the 3D probe behaves in the y dimension as it does in the x dimension due to the cylindrical symmetry of the 3D transducer. The accuracy of the simulation results could be validated by the resolution measurements for the x and z plane with the use of black microspheres (Fig. 4A).

3.3. Detection limits and signal stability in vitro

In a tissue mimicking phantom the limit of detection of a dilution series of live B16F10 cells acquired by the 2D probe was found to be 137 cells /μl PBS at 3 mm depth which was up to three folds lower than with the 3D probe (412 cells /μl PBS) (Fig. 5A and B). The cells could be detected by their signal difference to background in a brain tissue mimicking phantom up to a depth of 16.5 mm with the 2D probe and, thus, at least 2.5 mm deeper than with the 3D probe (limit of detection: 14 mm). The rather flat signal derived from tissue mimicking phantom background was found to be highest at the depth around the center of rotation of the

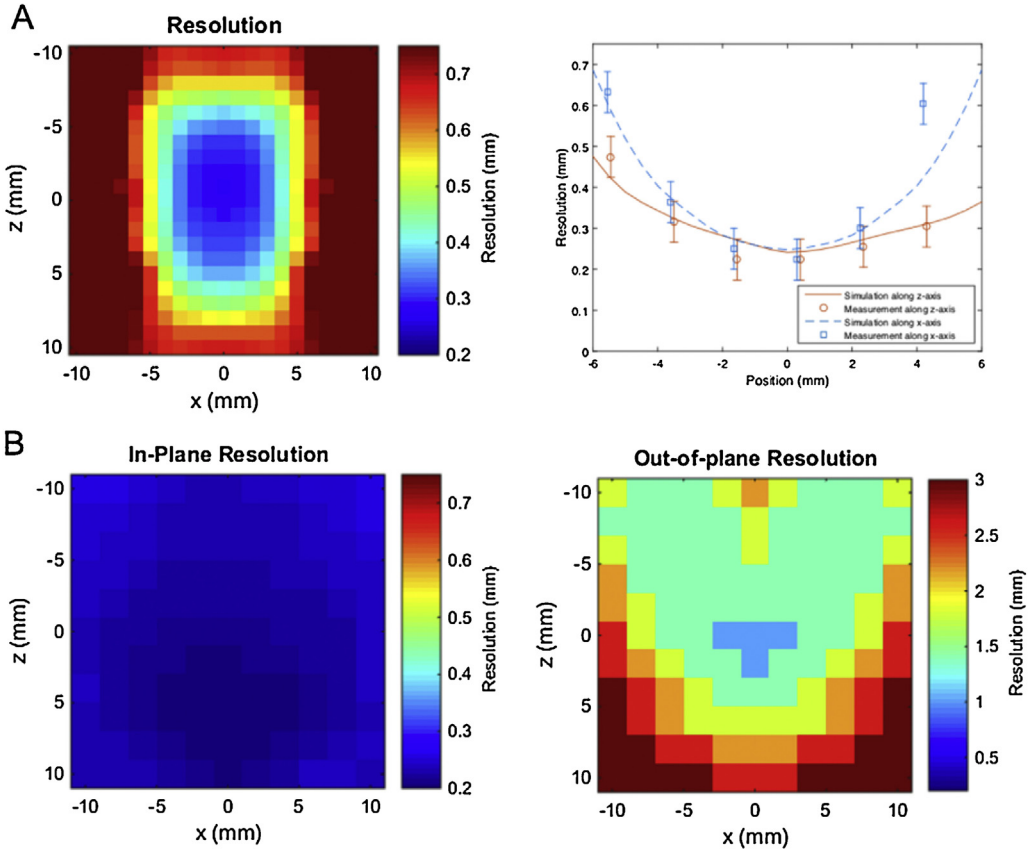

Fig. 4. A. 3D probe: The optimal resolution of the transducer, approximately 240 μm, is reached for target objects that are positioned ± 5 mm around the center of rotation. The resolution gradually decreases with respect to distance from the center of rotation in the z dimension as well as the x and y dimension due to the 3D detector elements' array. This relationship applies to the x and y dimension in equal terms due to the detector's cylindrical symmetry.
The simulation results were validated by the resolution being measured with the use of black microspheres around the center of rotation of the detector array along the x-axis and along the z-axis as previously described [16]. The resolution measurements were found to be in good agreement with the simulation results.
B. 2D probe: With regard to the 2D detector configuration, the in-plane resolution needs to be distinguished from the out-of-plane resolution due to its limit to two dimensions. The in-plane maximum resolution reaches up to 200 μm close to the center of rotation and remains stable below 300 μm in a range of ± 10 mm away from the center of rotation in the x and z plane. The out-of-plane resolution dramatically decreases beyond approximately ± 1 mm out-of-plane in the y dimension (slice thickness) with respect to the center of rotation.

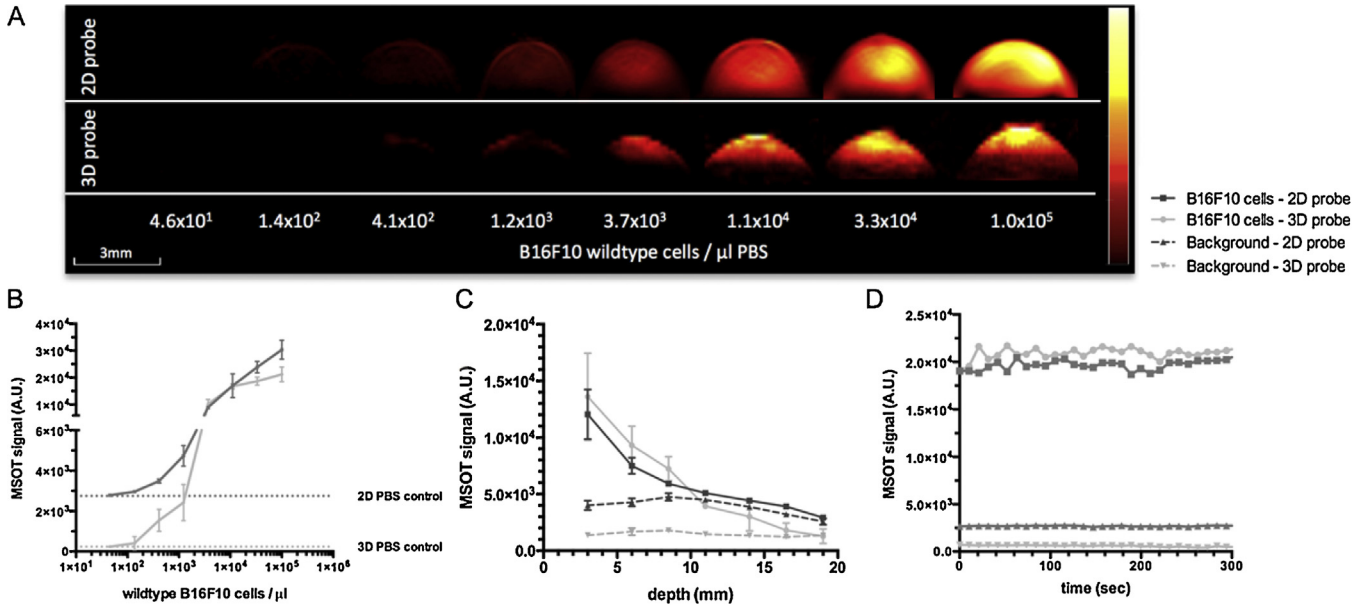

Fig. 5. A. Comparison of the detection threshold of the 2D and 3D probe: MSOT signal (shown as maximum intensity projection, MIP) at 800 nm of a dilution series of B16F10 cells in 20 µl PBS suspension inserted in a tissue mimicking phantom at 3 mm depth (scale: minimum to maximum). **B.** Signal to log-concentration plot of the detection threshold for the 2D- and 3D- probe (n = 3, error bars = SD): The lowest density of cells which yielded a MSOT signal that significantly differed from the PBS control solution (2D: 2750 ± 38 a.u.; 3D: 235 ± 28 a.u.) were 137 cells / µl with the use of the 2D probe (2960 ± 45 a.u., n = 3, $P < 0.05$) and 412 cells / µl with the 3D probe (1547 ± 545 a.u., n = 3, $P < 0.05$). **C.** MSOT signal of $7.4x10^4$ B16F10 cells in 20 µl suspension in relation to depth in a tissue mimicking phantom of increasing thickness (n = 3, error bars = SD). **D.** MSOT signal (at 800 nm) of $7.4x10^4$ B16F10 cells in 20 µl suspension and tissue mimicking phantom background (3 mm depth) at constant multituned laser irradiation (700-900 nm in 10 nm steps) for 5 minutes (2D ROI = 1.35 mm^2; 3D ROI = 1.16 mm^2).

probes, demonstrating the influence of the field of sensitivity characteristics of the probes on the signal intensity (Fig. 5C). Throughout continuous multispectral laser irradiation (700-900 nm) of 5 minutes the MSOT signal of the cell suspension as well as the phantom's background signal remained stable and no significant signal loss over time could be detected with either the 2D or the 3D probe ($P > 0.1$, Fig. 5D). Of note, the tissue mimicking phantom's normalized background MSOT signal itself was significantly higher when acquired with the 2D probe (2692 ± 44.2 a.u.) than with the 3D probe (587 ± 92 a.u., n = 30, $P < 0.001$) (Fig. 5D).

3.4. Accuracy and reliability in vivo

In vivo, both probes were capable of imaging the melanoma brain metastases at all time points qualitatively (Fig. 6A and Supplementary Figure S1). Quantitatively, throughout all three dimensions the tumor extent was found to be of significantly greater size when imaged with the 2D (x = 6.19 ± 1.10 mm; y = 3.17 ± 0.43 mm; z = 6.58 ± 1.40 mm) compared to the 3D probe (x = 3.95 ± 0.77 mm, $P < 0.05$; y = 1.98 ± 0.28 mm, $P < 0.01$; z = 3.68 ± 0.87 mm, $P < 0.05$, n = 4 each) when tumor sizes had reached a mean diameter of approximately 5.5 mm as depicted by MRI on day 13 post implantation (Fig. 6B, 6C and 7A). Tumors were confirmed as melanoma brain metastases by histological examination (Fig. 7B). Overall, in anatomical reference to MRI as standard in all 3 dimensions, the 2D probe proved more accurate in depicting the tumor extent with an overall bias of only 0.24 mm [95%-LA: -3.35 to 3.82] compared to the 3D probe (bias = 2.35 mm [95%-LA: -0.6 to 5.3]) (Bland-Altman plots, Fig. 6D). Of note, with regard to the 2D probe tumor extension beyond 4 mm in depth remarkably limited the accuracy in depth (z dimension), while the accuracy for the x and y dimensions was not affected by tumor size as such. With regard to the 3D probe, however, the accuracy was limited beyond a tumor size of 3.5 mm in all dimensions.

In terms of precision, the in vivo test-retest reliability was found to be comparably high for both approaches (2D: ICC = 0.97 [0.90 – 0.99]; 3D: ICC = 0.89 [0.69 – 0.97]) (Fig. 8). With regard to imaging acquisition time, the 3D-image acquisition was less time consuming than the 2D approach due to less image sets needed based on the simultaneous acquisition of the 3rd dimension: One image set per mouse and day (acquisition time ≈ 1 min, mean number of scans = 1) was sufficient to depict the tumor dimensions in total with the use of the 3D probe. The 2D probe required at least two different image sets with the need for repositioning the probe perpendicularly between scans (mean acquisition time = 8.1 ± 3.7 min, mean number of scans = 7.6 ± 2.3, n = 4, $P < 0.001$).

4. Discussion

We studied the performance of two recently developed optoacoustic handheld probes with real-time multispectral unmixing abilities, which were specifically developed with the aim of clinical translation in mind. However, the approach of image acquisition differs significantly between the two systems - the 2D probe and the 3D probe - which is reflected by the individual performance. All 2D- and 3D- handheld approaches for multispectral optoacoustic imaging that have been reported so far have been based on prototypical experimental setups that were, as such, not suitable for clinical applications. Such systems incorporated fewer detector arrays, provided less angular coverage and/or were more limited in resolution and imaging depth in real-time [13–16,22,23]. In addition, with regard to clinical translation, the laser energy level used to run those systems were either not explicitly reported, acquired or may not have met the maximum permissible laser energy exposure threshold according to the American National Standard for Safe Use of Lasers [17] as a similar laser source was used in some studies as in the setup reported here but

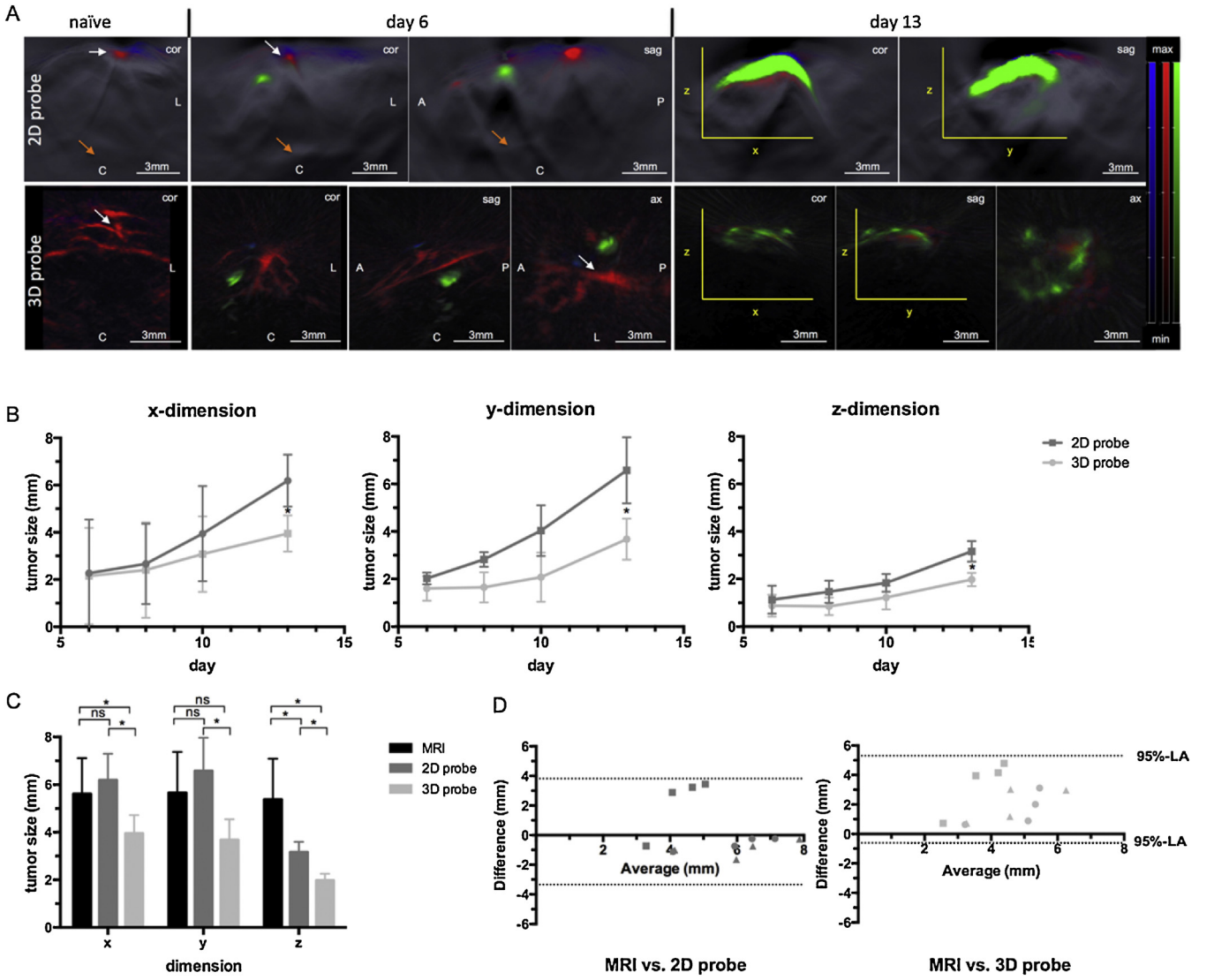

Fig. 6. A. In vivo MSOT images of a naïve and a melanoma bearing mouse brain acquired with the 2D probe (upper panel) and 3D probe (lower panel); shown are results at day 6 and day 13 after tumor inoculation (background wavelength = 860 nm; melanin = green; oxygenated hemoglobin = red; deoxygenated hemoglobin = blue; superior sagittal sinus = white arrow; skull base = orange arrow; A = anterior; P = posterior; C = caudal; L = left side; cor = coronal; sag = sagittal; ax = axial). While on day 6 the small spherical volume of the melanin-containing tumor is depicted in total with both approaches, the tumor size on day 13 seems to limit the capability to depict the tumor volume as a whole in both approaches due to saturation. **B.** Tumor size growth over time in days in the x, y, z dimensions (error bars = SD): While there was no significant difference in tumor size detected between both probes on day 6, when tumors were still small in size ($P > 0.1$), the difference in tumor size between the two probes increases gradually over time. On day 13 post implantation, the tumor size measured with the 2D probe was significantly greater in all three dimensions (x,y,z) than when measured with the 3D probe (* = $P < 0.05$). **C.** The mean tumor size measured with the 2D probe did not differ from the tumor size measured with T1-weighted MRI on day 13 post implantation regarding the x and y dimension ($P > 0.1$, ns = non-significant). With the regard to depth of the tumor (z dimension), the tumor size was found to be significantly greater on MRI than measured with either the 2D ($P < 0.05$) or the 3D probe ($P < 0.05$, error bars = SD). **D.** Bland-Altman plots of the accuracy of resembling the tumor extent on MSOT images acquired by the 2D and 3D probe, respectively, vs. MRI as a standard on day 13 (95%-LA = 95% limits of agreement; x dimension = •, y = ▲; z = ■).

no use of a mechanical attenuator or a PCD was disclosed to reduce the energy output accordingly [13,15,16].

According to our results, the 2D MSOT probe proved to be more suitable than the 3D MSOT probe for handheld optoacoustic imaging, particularly for highly absorbing and scattering tissue targets at greater depths with regard to accuracy, reliability and background signaling for spatial orientation. One might think that the depth correction function that was applied to the 2D data may have influenced the superior performance of the 2D probe at greater depth. However, the signal enhancement within the area where the target objects were placed was very subtle and limited to up to 10% relative to the uncorrected values and could as such be ruled out as a significant cause for the difference found in tumor assessments between the two probes (see Supplementary Figure S2). One reason for the disadvantage of the 3D probe regarding these performance metrics may be the geometrically suboptimal distribution of diffused light in the center of the detector array. This likely limits the accuracy and imaging depth in case of a strong light absorbing tissue target in the center of the FOV, such as the challenging melanoma brain metastasis model used in our study. On the other hand, the data for the 2D probe indicate strong potential for clinical applications in various scenarios, because the 2D probe enables 1) real-time handheld MSOT operation similar to diagnostic ultrasound imaging, and 2) fast wavelength tuning that allows excellent multispectral unmixing of optoacoustic contrast in real-time at satisfactory resolution and imaging depth. This provides enhanced background signal for spatial orientation and yields high accuracy as well as excellent test-retest reliability, even in optically challenging target tissues. However, the 3D approach reported here holds promise for

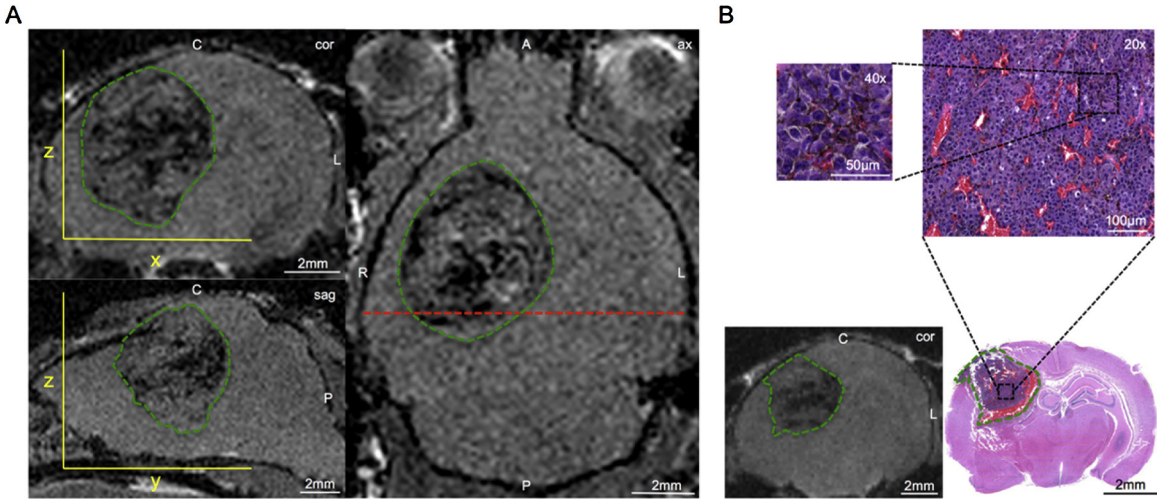

Fig. 7. A. A 3D isovoxel T1 FLASH MRI sequence (TE/TR = 5.5/35 ms) served as reference standard in vivo for tumor size evaluations (cor = coronal; sag = sagittal; ax = axial; R = right; L = left; A = anterior; P = Posterior; C = cranial). A lesion of varying intensity, mostly hypointense, could be identified at the site of implantation in all mice (dashed green line). The MRI data was verified by histological correlation (example given in Figure B: dashed red line = corresponding plane to coronal section in Figure B, dashed green line = tumor delineation). **B.** Histological examination with the use of hematoxylin & eosin (H&E) staining could confirm the presence of a highly vascularized melanoma brain metastasis (1x and 20x magnification). The brown pigment represents the typical appearance of focal deposition of melanin in a melanoma tumor (40x magnification).

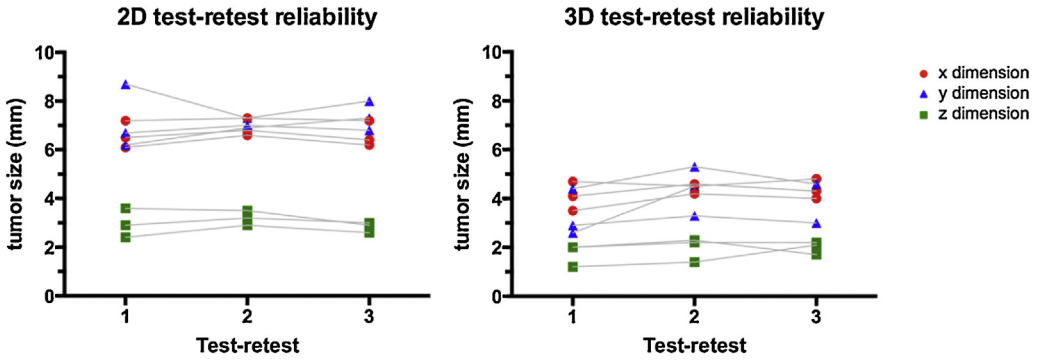

Fig. 8. Test-retest reliability: Each dot represents a single measurement of the maximum tumor extent in either the x, y or z dimension; each line connects to the respective retest value. The overall test-retest reliability was found to be excellent for the 2D probe (ICC = 0.97 [0.90-0.99]) as well as high for the 3D probe (ICC = 0.89 [0.69-0.97]).

more superficial applications, i.e. in the field of intraoperative use, dermatology, superficial angiography or soft tissues with less scattering and absorptive optical properties than brain and skull, i.e. breast or subcutaneous fat and lymphatic tissue. Importantly, immediate 3D visualization of the target tissue saves time [15,24]. As different clinical scenarios may demand different optoacoustic imaging approaches, this study expands the knowledge of such capabilities and limitations of the recently developed 2D and 3D MSOT handheld probes. With regard to clinical translation of the specific clinical scenario of melanoma detection our study was limited in providing data about the unspecific occurrence of unmixed melanin signal in biological tissues in the absence of neoplasm that could potentially affect its limit of detection in vivo. Overall, this study should help in further improving such MSOT systems in handheld operation on their way towards clinical translation.

5. Conclusions

Both the 2D and 3D handheld MSOT systems provide real-time multispectral unmixing and hold great promise for clinical translation. The 2D MSOT handheld probe was found to provide sufficient resolution and sensitivity as well as high accuracy and reliability, even in highly absorbing and scattering target tissues. In comparison, the 3D MSOT handheld probe added unique 3D capabilities shortening imaging time, but was more limited in its accuracy in scenarios with highly absorbing target tissues and at greater tissue depths. Overall, the data resulting from this study has identified specific strengths but also limitations of both systems, which should aid in further improving their performance before actual clinical translation begins.

Conflicts of interest

V.Neuschmelting, H.L., S.H. and M.F.K. have no conflicts of interest to declare and designed the study, acquired and held control of the data, performed the analyses and wrote the text submitted for publication. V.Ntziachristos has financial interest as a consultant and N.B. and A.U. are employees of iThera Medical, Munich, Germany.

Acknowledgements

The photoacoustic system was purchased with the help of a MSKCC Molecularly Targeted Intra-Operative Imaging Grant (M.F.K.); The study was further supported by the following grants:

NIH R01 EB017748 (M.F.K.); NIH K08 CA16396 (M.F.K.); M.F.K. is a Damon Runyon-Rachleff Innovator supported (in part) by the Damon Runyon Cancer Research Foundation (DRR-29-14); Pershing Square Sohn Prize (M.F.K.); RSNA Research Scholar Grant (M.F.K.); MSKCC Center for Molecular Imaging and Nanotechnology Grant (M.F.K.); MSKCC Experimental Therapeutics Grant (M.F.K.); MSKCC Technology Development Grant (M.F.K.); Geoffrey Beene Cancer Research Center Grant Award (M.F.K.); Society of MSKCC Research Grant (M.F.K.); Deutsche Forschungsgemeinschaft (DFG) Research Fellowship Grant NE 1922/2-1 (Volker Neuschmelting). Acknowledgments are also extended to the grant-funding support provided by the MSKCC NIH Core Grant (P30-CA008748).

Furthermore, we thank iThera Medical GmbH, Munich, Germany, for providing us with the 2D handheld probe used in this study. In particular, we thank Clinton Hupple and Marcin Kacprowicz, iThera Medical, for technical support. We also thank the Jan Grimm lab (MSKCC) for providing the melanoma cells.

The author portraits are provided together with the biographies.

Appendix A. Supplementary data

Supplementary data associated with this article can be found, in the online version, at doi:10.1016/j.pacs.2015.12.001.

References

[1] A. Taruttis, V. Ntziachristos, Advances in real-time multispectral optoacoustic imaging and its applications, Nat Photonics. 9 (2015) 219–227.
[2] V. Ntziachristos, Going deeper than microscopy: the optical imaging frontier in biology, Nature methods. 7 (2010) 603–614.
[3] X. Wang, X. Xie, G. Ku, et al., Noninvasive imaging of hemoglobin concentration and oxygenation in the rat brain using high-resolution photoacoustic tomography, Journal of biomedical optics. 11 (2006) 024015.
[4] N.C. Burton, M. Patel, S. Morscher, et al., Multispectral opto-acoustic tomography (MSOT) of the brain and glioblastoma characterization, Neuroimage. 65 (2013) 522–528.
[5] E.I. Galanzha, E.V. Shashkov, P.M. Spring, et al., In vivo, noninvasive, label-free detection and eradication of circulating metastatic melanoma cells using two-color photoacoustic flow cytometry with a diode laser, Cancer Res. 69 (2009) 7926–7934.
[6] N.C. Deliolanis, A. Ale, S. Morscher, et al., Deep-Tissue Reporter-Gene Imaging with Fluorescence and Optoacoustic Tomography: A Performance Overview, Mol Imaging Biol. (2014).
[7] S. Zackrisson, S.M. van de Ven, S.S. Gambhir, Light in and sound out: emerging translational strategies for photoacoustic imaging, Cancer Res. 74 (2014) 979–1004.
[8] J. Yao, J. Xia, K.I. Maslov, et al., Noninvasive photoacoustic computed tomography of mouse brain metabolism in vivo, Neuroimage. 64 (2013) 257–266.
[9] M.F. Kircher, A. de la Zerda, J.V. Jokerst, et al., A brain tumor molecular imaging strategy using a new triple-modality MRI-photoacoustic-Raman nanoparticle, Nat Med. 18 (2012) 829–834.
[10] J. Laufer, P. Johnson, E. Zhang, et al., In vivo preclinical photoacoustic imaging of tumor vasculature development and therapy, Journal of biomedical optics. 17 (2012) 056016.
[11] E. Herzog, A. Taruttis, N. Beziere, et al., Optical imaging of cancer heterogeneity with multispectral optoacoustic tomography, Radiology. 263 (2012) 461–468.
[12] A. Taruttis, M. Wildgruber, K. Kosanke, et al., Multispectral optoacoustic tomography of myocardial infarction, Photoacoustics. 1 (2013) 3–8.
[13] A. Buehler, M. Kacprowicz, A. Taruttis, et al., Real-time handheld multispectral optoacoustic imaging, Opt Lett. 38 (2013) 1404–1406.
[14] Y. Zhou, W. Xing, K.I. Maslov, et al., Handheld photoacoustic microscopy to detect melanoma depth in vivo, Opt Lett. 39 (2014) 4731–4734.
[15] X.L. Dean-Ben, D. Razansky, Functional optoacoustic human angiography with handheld video rate three dimensional scanner, Photoacoustics. 1 (2013) 68–73.
[16] X.L. Dean-Ben, D. Razansky, Portable spherical array probe for volumetric real-time optoacoustic imaging at centimeter-scale depths, Optics express. 21 (2013) 28062–28071.
[17] L.I.o. America, American National Standard for Safe Use of Lasers. ANSI Z1361., Laser Institute of America;, Orlanda, FL, USA, 2007p. 249.
[18] S.L. Jacques, Optical properties of biological tissues: a review, Physics in medicine and biology. 58 (2013) R37–R61.
[19] R. Cubeddu, A. Pifferi, P. Taroni, et al., A solid tissue phantom for photon migration studies, Physics in medicine and biology. 42 (1997) 1971–1979.
[20] J.J. Bartko, The intraclass correlation coefficient as a measure of reliability, Psychological reports. 19 (1966) 3–11.
[21] J.M. Bland, D.G. Altman, Statistical methods for assessing agreement between two methods of clinical measurement, Lancet. 1 (1986) 307–310.
[22] M. Heijblom, D. Piras, W. Xia, et al., Visualizing breast cancer using the Twente photoacoustic mammoscope: what do we learn from twelve new patient measurements?,, Optics express. 20 (2012) 11582–11597.
[23] C. Kim, T.N. Erpelding, K. Maslov, et al., Handheld array-based photoacoustic probe for guiding needle biopsy of sentinel lymph nodes, Journal of biomedical optics. 15 (2010) 046010.
[24] R.A. Kruger, C.M. Kuzmiak, R.B. Lam, et al., Dedicated 3D photoacoustic breast imaging, Medical physics. 40 (2013) 113301.

Volker Neuschmelting studied Medicine at the University of Bonn, Germany, at the Institute of Neurology, Queen Square, at UCL London and at the University Hospital Berne, Switzerland before he received his medical doctorate from the University of Berne, Switzerland. He joined the University Hospital Cologne, Germany, for his residency in neurosurgery and focused his research activities on advanced pre- and intraoperative neuroimaging techniques in brain cancer patients. In his current position as research fellow in the Kircher Lab, Department of Radiology, Memorial Sloan Kettering Cancer Center, he persues the development of optical imaging techniques, in particular photoacoustics and Raman spectroscopy, for translation in neurooncology.

Neal Burton received his doctorate from the Division of Toxicology, Johns Hopkins Bloomberg School of Public Health. He is currently an Application Specialist at iThera Medical. He is also a Guest Scientist at the Institute for Biological and Medical Imaging at the Helmholtz Center in Munich, Germany. His main activities at iThera Medical include oversight of application development of optoacoustic clinical imaging as well as the publication of preclinical optoacoustic imaging studies in pharmacology and cancer models in small animals.

Hannah Lockau studied Medicine at the Technical University Munich, Germany, at the Sydney Medical School, Australia and at the Institute of Neurology, Queen Square, at UCL London. She did her residency in Radiology at the Department of Radiology, University Hospital Cologne, Germany and received her medical doctorate degree before she joined the Department of Radiology at the Memorial Sloan Kettering Cancer Center, in her current position as research fellow. Her main research interests include multimodal advanced imaging techniques by means of PET/MRI and optical modalities such as Cerenkov and photoacoustic imaging.

Alexander Urich studied physics at the University of Heidelberg, Germany, and University of Oklahoma, before he received his doctorate degree in physics and electrical engineering at the Technical University of Vienna, Austria. He now works as a Research and Development engineer on optoelectronics and acoustics at iThera Medical.

Stefan Harmsen received his M.S. in Chemistry from the Free University Amsterdam and a PhD in Toxicology from Utrecht University, Netherlands. He then joined the Kircher Lab at Memorial Sloan Kettering Cancer Center. As a Research Associate, he currently develops novel nanoparticle-based materials and optical imaging modalities for cancer imaging. These modalities include surface-enhanced resonance Raman scattering (SERRS) imaging, near-infrared fluorescence, and photoacoustics. By establishing straightforward nanoparticle surface modification protocols, which allow conjugation of polymers, targeting peptides, and contrast agents, he developes nanoparticle-based multimodal imaging strategies for highly sensitive cancer imaging.

Vasilis Ntziachristos studied electrical engineering at Aristotle University in Thessaloniki, Greece and received his Master's and Doctorate degrees from the Bioengineering Department of the University of Pennsylvania, USA. After completing a postdoc at the Center for Molecular Imaging Research (CMIR) at Harvard Medical School, he served as an instructor and then assistant professor and director of the Laboratory for Bio-Optics and Molecular Imaging at Harvard University and Massachusetts General Hospital, Boston, USA. He is currently a Professor of Medicine, Professor of Electrical Engineering and Chair for Biological Imaging (CBI) at the Technical University Munich and the Director of the Institute for Biological and Medical Imaging (IBMI) at the Helmholtz Zentrum Munich, Germany. His research concentrates on basic research and translation of novel optical and optoacoustic in vivo imaging for addressing unmet biological and clinical needs.

Moritz Kircher studied Medicine in Würzburg, Berlin, Paris, and at Harvard. He received his doctorate from the Humboldt University in Berlin. He completed a residency in Diagnostic Radiology and a postdoc in molecular imaging at Harvard Medical School, a clinical MRI fellowship at Stanford University Medical Center, and a postdoc at the Molecular Imaging Program at Stanford. He is now an Assistant Professor, director of the Kircher Lab, and a Member of the Center for Molecular Imaging and Nanotechnology (CMINT) at Memorial Sloan Kettering Cancer Center. His laboratory focuses on the development of methods that allow combined pre- and intraoperative high precision tumor visualization, to which end he develops novel multimodal nanoparticle probes based on surface-enhanced resonance Raman spectroscopy (SERRS), photoacoustic and MR imaging.